Clays and Clay Minerals, Vol. 53, No. 5, 452–465, 2005.

CHARACTERIZATION AND ORIGIN OF Fe^{3+}-MONTMORILLONITE IN DEEP-WATER CALCAREOUS SEDIMENTS (PACIFIC OCEAN, COSTA RICA MARGIN)

A. Gaudin[1], M. D. Buatier[2], D. Beaufort[3], S. Petit[3], O. Grauby[4] and A. Decarreau[3]

[1] CNRS-UMR 6112, Laboratoire de Planétologie et Géodynamique, Faculté des Sciences et Techniques, Université de Nantes, BP 92208, 44322 Nantes Cedex 03, France

[2] Département de Géosciences, EA2642, UFR Sciences et Technique, Université de Franche Comté, 16 Route de Gray, 25065 Besançon, France

[3] CNRS-UMR 6532, Laboratoire HydrASA, Faculté des Sciences, 86022 Poitiers Cedex, France

[4] CRMC2, CNRS-UPR 7251, Campus de Luminy, Case 913, F-13288 Marseille Cedex 09, France

Abstract—Millimetric to centimetric green grains widespread in pelagic calcareous sediments recovered at a water depth of 3000 m near the Costa Rica margin were studied by X-ray diffraction, scanning electron microscopy (SEM), transmission electron microscopy (TEM) and Fourier transform infrared spectroscopy. Samples were collected, during the *Ticoflux II* expedition, from the upper bioturbated part of four sedimentary cores (0.13–3.75 m below seafloor). The sediments are calcareous and siliceous nanofossil oozes (coccoliths, diatoms, radiolarians, *etc.*).

Green grains show generally a concentric zoning with a green rim in which smectite largely predominates over pyrite and a black core in which pyrite is prevalent. Observations by SEM indicate that this zoning results from a progressive inward alteration and replacement of the accumulations of pyrites by smectites. The high-resolution TEM observations of the smectite-pyrite interfaces suggest that the replacement of pyrites by smectite occurs through a dissolution-precipitation process with the formation of a gel. The pyrite matrix is composed of a huge number of very small (0.5–2 μm) pyrite octahedra, a typical texture resulting from the pyritization of organic material in early diagenetic environments.

The accurate mineralogical and crystal chemical characterization of the smectites indicate that they are Fe^{3+}-montmorillonites (Fe^{3+}-rich smectite with a dominant octahedral charge, rarely recorded in the literature). The formation of such Fe^{3+}-montmorillonites forming green grains could be explained by two successive diagenetic redox stages: (1) reducing stage: early pyritization of the organic matter by microbial reduction within reducing micro-environments; (2) oxidizing stage: Fe^{3+}-montmorillonite crystallized in space liberated after dissolution of pyrite connected with the rebalancing of the redox conditions of the micro-environments with the oxidizing surrounding sediments.

Key Words—Calcareous Sediments, Costa Rica Margin, Montmorillonite, Pyrite, Smectite.

INTRODUCTION

The formation of clayey green grains in modern superficial marine sediments is a common process which is reported as "verdissement" in the literature (Odin and Morton, 1988). Thus, "verdine" and "glaucony" are the two main types of facies in which such a process is observed. For both facies, green grains form through early diagenetic processes at the sea water-sediment contact. Many types of substrates serve as templates for their growth, but carbonate tests, clayey fecal pellets, infillings of foraminiferal tests and various mineral grains and rock fragments are the most common (Odin and Matter, 1981). Green grains from the two facies present quite a similar aspect and are often optically indistinguishable. However, they differ by their mineralogical and chemical nature and their marine environments of formation.

The verdine facies comprises green grains composed of a mixture of di-trioctahedral Fe^{3+}-rich, 1:1 clay minerals (7 Å) which are sometimes associated with a 14 Å phase (Odin and Morton, 1988). It typically forms in warm tropical sea water (>20ºC, most often >25ºC) near river mouths at water depths between 10 and 60 m.

Glaucony refers to a petrographic facies in which green grains of glauconite (Fe^{3+}-, K^{+}-rich phyllosilicate family with "glauconite smectite" and "glauconite mica" as end-members; Odin and Matter, 1981) are abundant. Glauconitization processes occur over a wide latitudinal range 65ºN to 55ºS, and typically form at the outer part of the continental shelf, in water depths between 60 and 500 m (Odin and Morton, 1988) at temperatures near 15ºC (Odin and Fullagar, 1988). For this reason, they are commonly used for paleoenvironmental and paleoceanographic reconstruction. However, more rarely, the formation of glaucony has been locally reported in deep-water (up to 2500 m) sediments (Odin and Morton, 1988). Indeed, Wiewióra *et al.* (2001) and Giresse and Wiewióra (2001) described a glauconitization process at 2100 m water depth and at 3ºC in superficial sediments on the Ivory Coast-Ghana Ridge.

* E-mail address of corresponding author:
martine.buatier@univ-fcomte.fr
DOI: 10.1346/CCMN.2005.0530503

To date, very few accurate studies have been carried out on green grains formed in deep-water superficial marine sediments. Therefore, the present study focused on petrography, mineralogy and crystal chemical characterization of the authigenic clays forming green grains in marine pelagic carbonated sediments at 3000 m water depth, in the first meters below the sea floor. The results of this study will be used to support a discussion on both the origin and the mechanism of formation of the clay minerals which at present constitute the green grains in deep-sea conditions.

GEOLOGICAL SETTING

The samples studied come from sediment cores recovered at a water depth of 3000 m during the *Ticoflux II* expedition (2002) in the Costa Rica margin offshore of the Nocoya Peninsula (Figure 1). The Cocos plate has a complex tectonic history in this area, comprising seafloor generated at the EPR (East Pacific Rise) at a fast spreading rate and the CNS (Cocos-Nasca Spreading Center) at an intermediate spreading rate. In the investigated area, the crust has common seamounts that play a major role in sea water circulation in this off-axis system (Fisher *et al.*, 2003). The results from ODP Hole1039 drilling hole in the same area documented that the sedimentary cover is ~450 m thick. The upper 150 m are composed of hemipelagic mudstone (Pliocene and Pleistocene) and pelagic nanofossil oozes (Miocene) in the lower section. The sedimentation rate is ~46 m/m.y. for the Pleistocene and 6 m/m.y. for the late Miocene and Pliocene interval. The sediment types vary spatially in the *Ticoflux II* area in response to seafloor relief (topography), continental proximity and bottom currents.

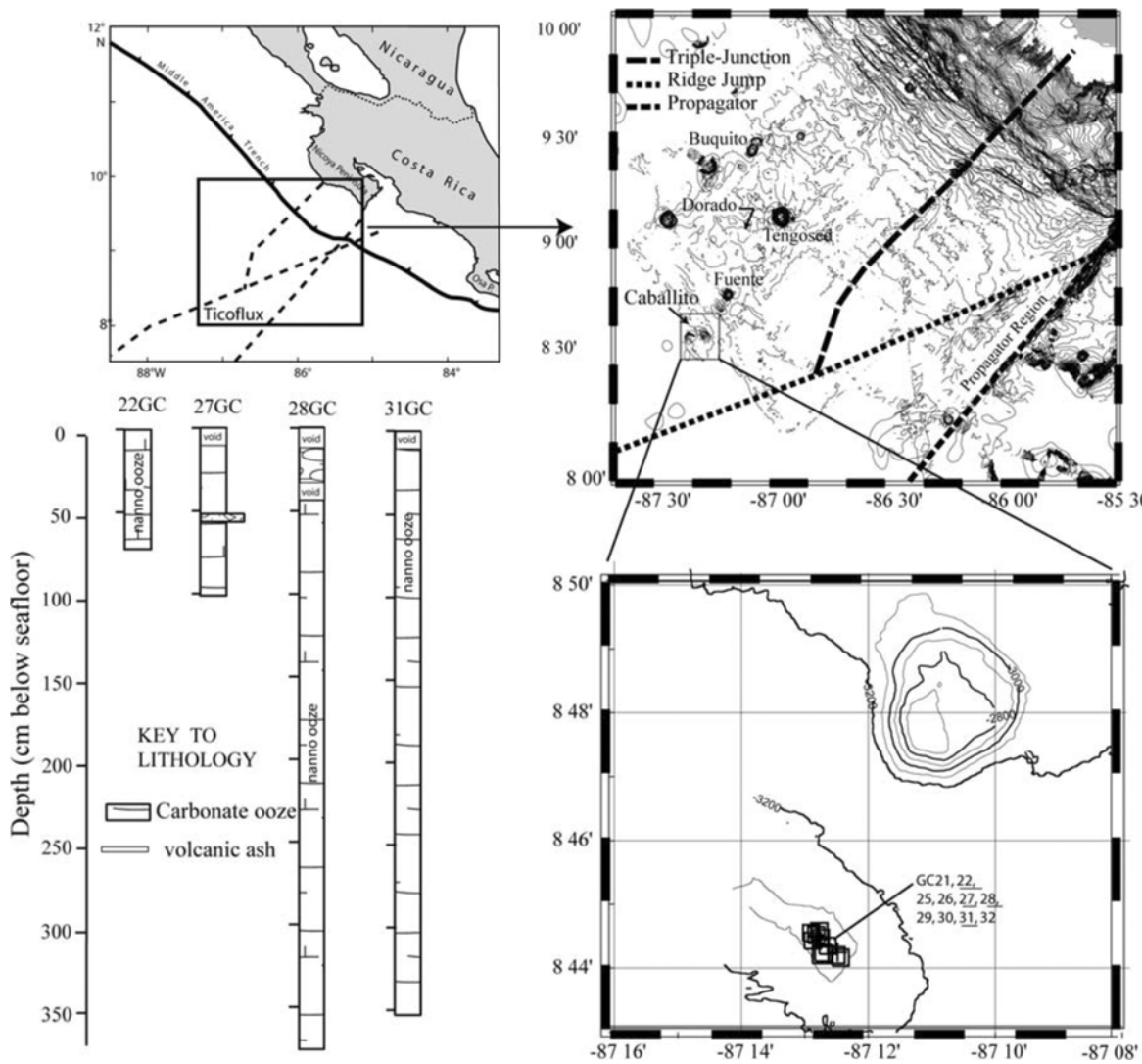

Figure 1. Location of the studied samples and schematic presentation of the studied cores. General map modified from Fisher *et al.* (2003).

https://doi.org/10.1346/CCMN.2005.0530503 Published online by Cambridge University Press

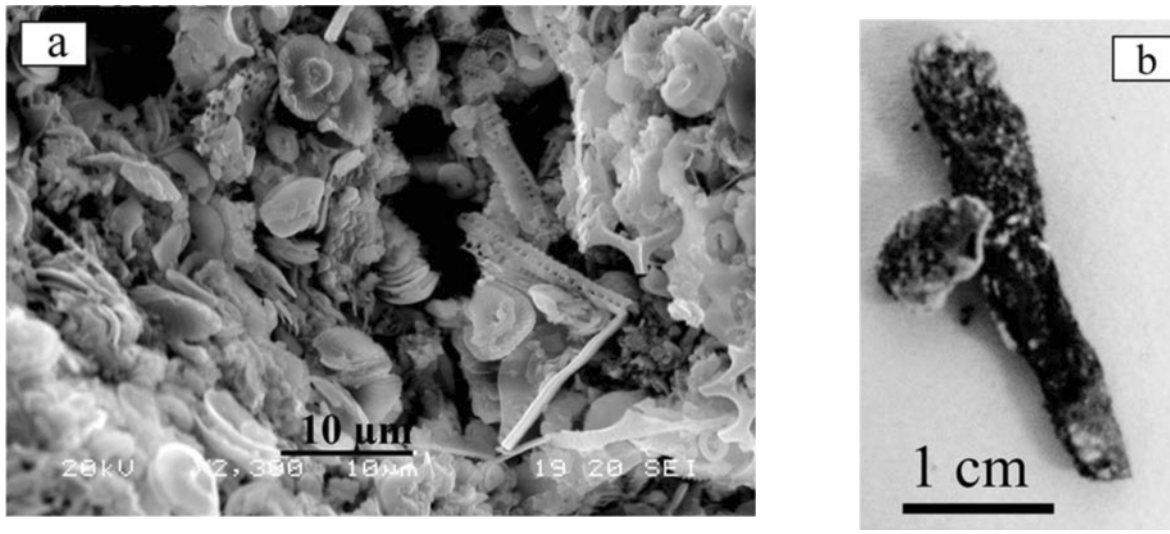

Figure 2. SEM images (a) of the carbonated biogenic ooze (sample 31-13) and (b) burrow fill by green and black product.

The sediments of the studied cores are dominated by calcareous oozes (chalk) composed of an assemblage of coccoliths with siliceous sponges spicules, diatoms and radiolarian fossil remains (Figure 2a). Mn-Fe oxide concretions or nodules are common on top of sedimentary cores. Sampling has been focused on millimetric to centimetric grains sometimes showing a burrow form and which are widespread in the calcareous sedimentary column (Figure 2b). These grains, referred to hereafter as the green grains, for brevity, have an average size which ranges from 1 mm to 1 cm and generally show a concentric zoning with a green rim and a black core.

MATERIALS AND METHODS

Eight samples were collected from the upper part of four cores, at depths varying from 0.13 to 3.75 m below the sea floor (Table 1). The shallower sample (31-13) comprises homogeneous pelagic calcareous oozes whereas the other, deeper samples systematically contain some disseminated green grains. The green grains were extracted mechanically from the pelagic carbonated sediments under a binocular lens. As much as possible, the green materials from the rim of the grain (27-52R) were separated from the inner black materials (27-52C) in order to develop a comparative mineralogical and textural study.

The <2 µm clay fractions were extracted from the bulk samples by centrifugation (Jouan© GR 422), sedimentation procedures and a mild decarbonation treatment using an acetic acid solution buffered to pH 5 with sodium acetate.

Scanning and transmission electron microscopy

Detailed petrographic observations of gold-coated rock fragments were performed using a scanning electron microscope (SEM Jeol 5800) equipped with an EDX system.

Fragments of green grains with black cores were impregnated following the procedure established by Tessier (1984) and Elsass *et al.* (1998) which consists

Table 1. XRD mineralogy and location of the studied samples (bulk samples). Smt: smectite; Gyp: gypsum; Calc: calcite; Pyr: pyrite; Hal: halloysite; Br: barite; Opl: opal; (+): in trace amount.

Core	Depth below sea floor (cm)	Sample	Smt	Gyp	Calc	Pyr	Hal	Br	Opl
Pelagic sediment									
31GC	13	31-13			+			+	+
Green grains with black cores from pelagic calcareous oozes									
22GC	40-73	22-40	+	(+)	+	+			
27GC	52-56	27-52R	+	(+)	+	+			
27GC	52-56	27-52C	+		(+)	+			
28GC	340	28-340	+		+		+		
28GC	341-375	28-375	+		+	+			
31GC	76	31-76	+		+				
31GC	240	31-240	+		+	+	+		

https://doi.org/10.1346/CCMN.2005.0530503 Published online by Cambridge University Press

of progressive exchanges of the interstitial water with alcohol, solvent and then Spurr resin. Ultrathin sections were obtained by ultramicrotomy using a diamond knife and their high-resolution TEM (HRTEM) observations were made on a TEM Jeol® 2000FX, at CRMC2, Marseille. Chemical analyses of clay particles sedimented on collodion-carbon-coated copper grids were performed using the EDX system of the same TEM.

X-ray diffraction (XRD)

For XRD analyses, a Philips® PW 1729 diffractometer equipped with a Cu tube (operated at 40 kV, 40 mA) and a graphite monochromator was used. The XRD patterns were obtained on powders and on air-dried, ethylene glycol-saturated (EG), heated (390ºC for 4 h) and oriented Ca^{2+}-saturated clay fractions. The swelling properties of the clays were studied using ethylene glycol saturation after the Hofmann and Klemen (1950) (HK) procedure which consists of: (1) total exchange of the exchangeable cations by Li cations; and (2) heating at 250ºC for 12 h. This procedure involves the neutralization of the electric charge resulting from the non-equivalent isomorphous substitutions into the octahedral sheets by Li cations coming from the interlayer position. After HK treatment, the layers having a tetrahedral charge of <0.18 per half unit-cell cannot swell (*i.e.* d_{001} = 9.5 Å) whereas the layers with a tetrahedral charge exceeding 0.18 per half unit-cell are still expandable (Petit *et al*., 2002). The terminology 'HK swelling' and 'HK nonswelling' layers will be used hereafter to refer to both types of smectite layers distinguished above. The XRD diagrams were recorded using a counting time of 3 s per step of 0.02º2θ. For the study of the 06,33 reflections, powder XRD patterns were recorded using 15 s per step of 0.01º2θ, from 70 to 80º2θ with LiF as an internal reference. To improve the measurement of the positions of the diffraction peaks, XRD patterns were decomposed into elementary Gaussian curves using the *DECOMPXR* program (Lanson, 1993).

Fourier transform infrared spectroscopy

A Nicolet 510 FTIR spectrometer was used to record FTIR spectra at 4 cm^{-1} resolution in the 4000–400 cm^{-1} (MIR) region. The spectrometer was continuously purged with dry air during scanning of the transmission spectra. The KBr pellets were prepared by mixing 1 mg of sample with 150 mg of KBr and heated overnight at 110ºC in order to evacuate the hygroscopic water. The distribution of the smectite layer charge was measured by infrared (IR) spectroscopy on NH_4-saturated samples using the method of Petit *et al*. (1998).

RESULTS

Petrography and bulk mineralogy

According to SEM observations, the pelagic sediments largely comprise calcareous coccoliths (Figure 2a). Other biogenic particles include diatoms, radiolarians, sponge spicules and, locally, foraminifers and discoasters. The XRD study (Figure 3a, Table 1) of the sediment indicates that its mineralogy is broadly dominated by calcite. Moreover, analysis of the decarbonated sediment revealed significant amounts of opal, probably related to the siliceous biogenic elements mentioned previously (diatoms, radiolarians and sponge spicules), and minor barite.

The bulk mineralogy of the green grains is essentially composed of smectite, pyrite and residual calcite. The mineralogical compositions of both the green and black zones of the green grains differ mostly by the relative amounts of pyrite and smectite (Figure 3b). Pyrite predominates over smectite in the black core (27-52C), whereas smectite is largely dominant in the green rims (27-52R). Minor amounts of gypsum were also detected in the green rims.

The XRD patterns of the smectite are very similar in both the black and green zones. They present an intense 001 reflection at ~12 Å (Figure 3b) characteristic of smectite layers having one water layer in the interlayer position (Suquet *et al*., 1981a, 1981b).

Observations by SEM of cross-sections through the green grains corroborate the mineralogical results obtained from XRD analyses and indicate that the present zoning results from the progressive inward alteration and replacement of the accumulations of pyrite crystals by smectites associated with minor amounts of gypsum and of unidentified Fe oxides or hydroxides (Figure 4). Three successive zones were distinguished, each one corresponding to a different grade of the overall smectite precipitation and pyrite dissolution process.

Inner zone. The pyrite matrix is composed of a huge number of very small (0.5–2 μm) pyrite octahedra (Figure 4a). This texture has already been described for diagenetic pyrite from marine rocks and is usually considered to be the result of the complete pyritization of organic material (McKay and Longstaffe, 2003). Moreover, framboidal pyrites are observed locally (not shown in Figure 4). Detailed observations of pyrite octahedra at greater magnification reveal dissolution pits and rounded edges in the pyrite and incipient development of clay coatings which partly fill the pores (Figure 4b). The clay particles display the typical folded thin film morphology of smectites.

Intermediate zone. The pyrite matrix is more strongly dissolved and the smectite material is much more abundant than previously reported in the inner zone of the grains. All the pyrite octahedra are more or less dissolved (Figure 4c) and the newly formed smectite coatings are extensively developed in the residual pore space (Figure 4d). Locally, globular particles of undetermined Fe oxide or hydroxide are associated with the smectite films (Figure 4d).

https://doi.org/10.1346/CCMN.2005.0530503 Published online by Cambridge University Press

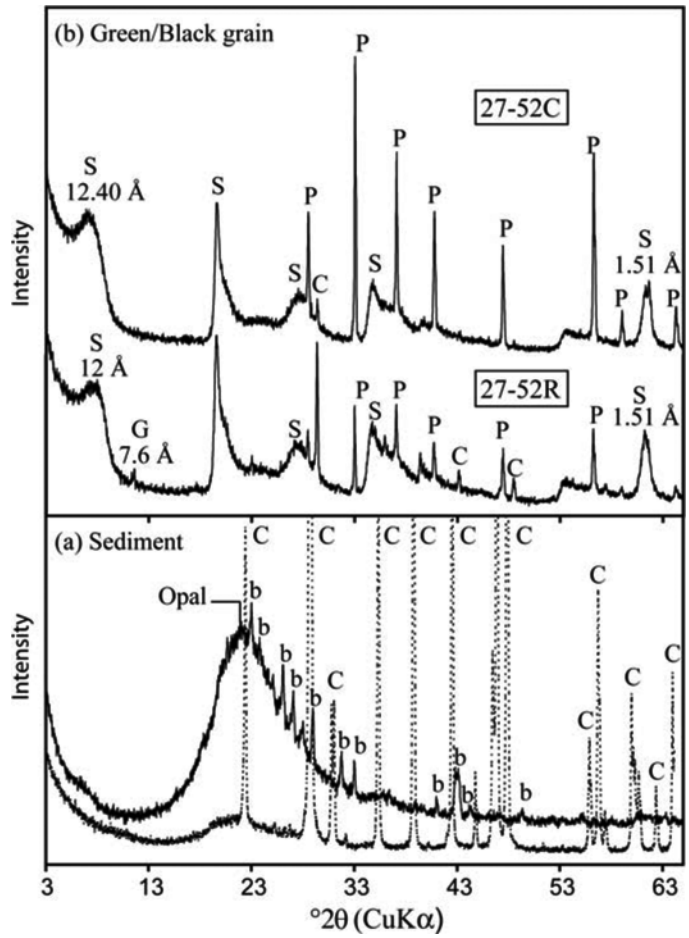

Figure 3. Powder XRD patterns of (a) the carbonated biogenic ooze (sample 31-13) before decarbonation (thin line) and after decarbonation (thick line) and (b) of sample 27-52R (green rim material of the grains) and of sample 27-52C (black core material). b: barite, C: calcite, S: smectite, G: gypsum, P: pyrite.

Outer zone. The earlier pyrite matrix has been almost totally replaced by smectite spherules (Figure 4e). Both the size and morphology of the smectite spherules seem to be inherited from those of the previous pyrite crystals. At higher magnification, it can be seen that smectites display a typical honeycomb structure (Figure 4f). Marked dissolution features, pseudomorphs of biogenic elements and invasion of the total porosity by the smectite matrix characterize the textural transformation of the host calcareous sediments close to the green grains (Figure 4g).

Using TEM, cross-sections of the inner zone of the grains allow the observation of the smectite-pyrite contact. The alteration front around the pyrite is marked by a thin layer of poorly crystallized or amorphous matter unstable under the electron beam (Figure 5a). This suggests that pyrite dissolution and the smectite precipitation which follows occur *via* a gel precusor.

Crystal structure and crystal chemistry of smectite

HRTEM study. Close to the pyrite relics (Figure 5a), the smectite particles display very diffuse boundaries and blurred 001 fringes with numerous discontinuities. Most of the crystallites oriented perpendicularly to *c** display fewer than five stacked layers.

The individual crystallites of the smectite tactoids observed farther from the pyrite relicts comprise packets of four to 15 stacked layers (Figure 5b). The pseudo-annular to slightly punctuated microdiffraction patterns obtained on these crystallites are characteristic of highly disordered, turbostratic stacking of smectite 00l layers with random rotations about *c**.

XRD study. The XRD patterns of randomly oriented powders of smectite exhibit asymmetrical (*hk*) reflections near 4.5 and 2.5 Å, indicative of a turbostratic stacking layer. Moreover, the unusual 06,33 reflection at 1.513 Å is characteristic of Fe^{3+}, Mg-rich dioctahedral smectites (Petit *et al*., 2002; Gaudin *et al*., 2004a).

All the XRD patterns of oriented preparations of Ca^{2+}-saturated smectite fractions collected within the green grains are very similar to those presented in Figure 6a. The XRD patterns of air-dried preparations show an intense 001 reflection near 14.6 Å which is

https://doi.org/10.1346/CCMN.2005.0530503 Published online by Cambridge University Press

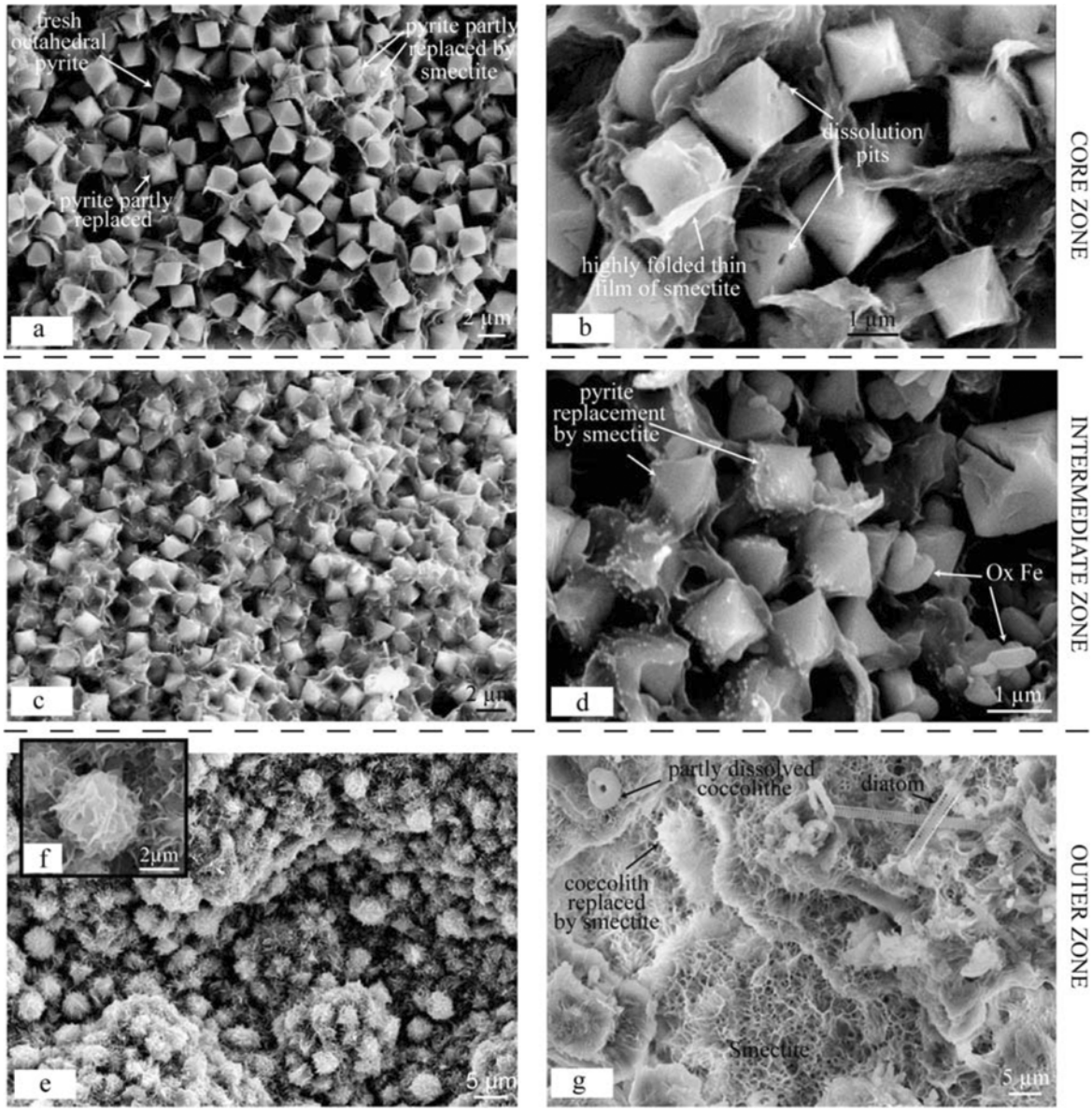

Figure 4. SEM images of grains extracted from the pelagic carbonated sediments, from the cores to the rims of the grains.

characteristic of smectite layers having two water layers in the interlayer position (Suquet *et al.*, 1981a, 1981b). After heating at 390ºC, the 001 reflection collapsed to 9.70 Å. After EG saturation, the 001 reflection shifts to 16.9 Å and two asymmetrical complex peaks near the positions of the harmonic 002 and 003 reflections (Figure 6b). The first diffraction profile has been fitted using two Gaussian peak shapes corresponding to 8.59 Å and at 9.13 Å *d* values. The first one is almost harmonic with d_{001} and has been attributed to the 002 reflection of a fully expandable smectite. The second one is a 002/001 reflection of a random mixed-layer phase composed of non-expandable phyllosilicate layers (d_{001} = 10 Å) with smectite layers, the interlayer cation of which is hydrated with two sheets of ethylene glycol (d_{00} = 17 Å). In the same way, the second diffraction profile has been fitted using two Gaussian peak shapes corresponding to 5.6 Å and 5.3 Å *d* spacings corresponding to the 003 diffraction peak of the fully expandable smectite and to the 003/002 reflection of the random mixed-layer phase already mentioned above, respectively. We should note that the nature of non-swelling layers involved in the mixed-layer phase is not clearly identified. It could correspond either to illite, glauconite or to smectite layers collapsed at 10 Å, and it will be discussed in the following section. The proportions of non-swelling layers were estimated at ~50% in the random mixed-layer phase from the comparison of

https://doi.org/10.1346/CCMN.2005.0530503 Published online by Cambridge University Press

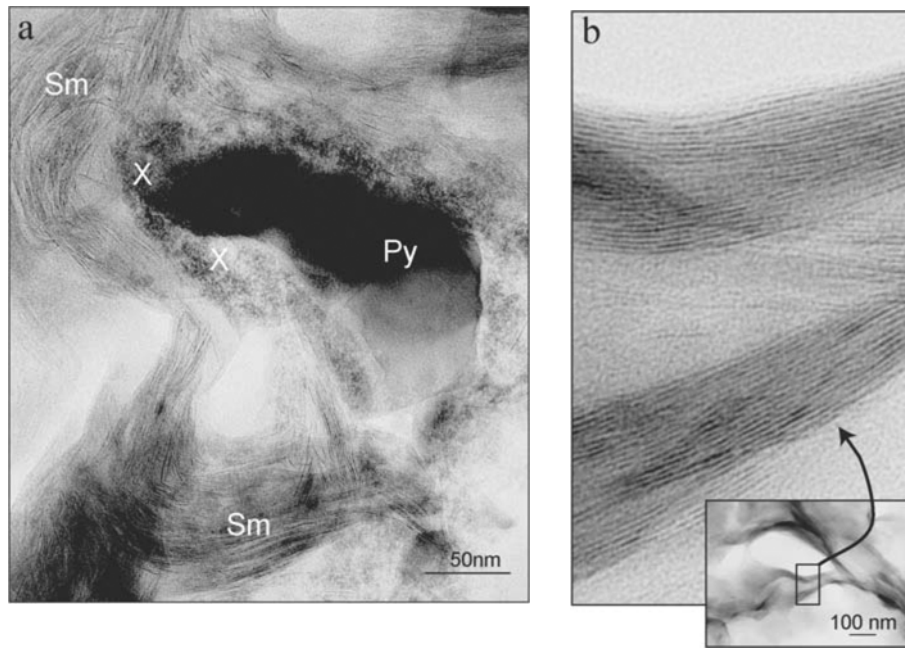

Figure 5. (a) TEM image of the smectite-pyrite interface and (b) low-magnification and high-resolution TEM images of smectites in sample 27-52. Sm: smectite, Py: pyrite, X: poorly crystallized phase.

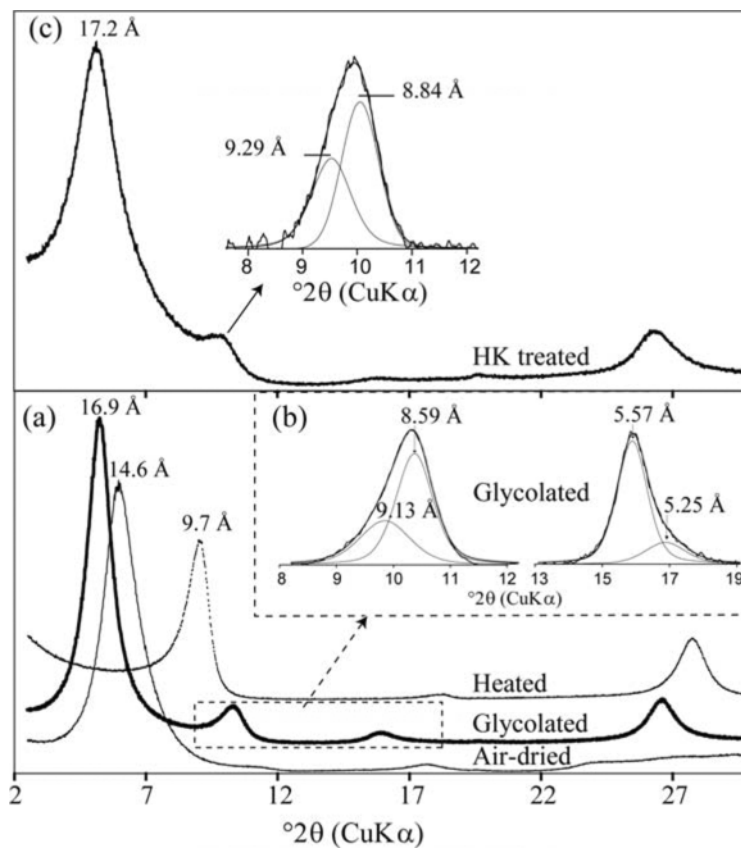

Figure 6. XRD patterns of (a) oriented Ca^{2+}-saturated smectite preparations (<2 μm fraction) from the 27-52GR smectite sample: air-dried, glycolated and heated. (b) Fitting of the 8–12°2θ and 13–19°2θ reflection bands of the glycolated preparation using the *DECOMPXR* program. (c) XRD pattern of the glycolated HK-treated sample 27-52GR and fitting of the 8–12°2θ reflection band.

https://doi.org/10.1346/CCMN.2005.0530503 Published online by Cambridge University Press

the experimental position of the 002/001 reflection with *NEWMOD* pattern simulations (Reynolds, 1985) of dioctahedral Fe-rich smectite-illite-like mixed layers.

After HK treatment and ethylene-glycol saturation (Figure 6c), the XRD patterns of smectite display an intense peak at 17.2 Å indicating that most of the smectite layers remain expandable. An asymmetric diffraction peak profile, well fitted with two Gaussian peak shapes at 8.84 Å and 9.29 Å, is still observed in the 8−12°2θ angular range. Both these *d* values are non-harmonic of d_{001} and greater than those reported for the glycolated clay fractions before the HK treatment (*i.e.* 8.59 Å, 9.13 Å). This suggests the presence of HK non-swelling layers in the clay particles. Thus, the first component at 8.84 Å is attributed to smectite crystallites in which two types of smectite layers are mixed layered: (1) HK non-swelling layers with low tetrahedral charges (<0.18); and (2) HK swelling layers with high tetrahedral charges (>0.18). The second component at 9.29 Å is attributed to crystallites in which three types of smectite layers are mixed layered: (1) HK swelling smectite layers; (2) HK non-swelling smectite layers; and (3) non-swelling layers (detected before HK treatment).

AEM analyses of individual particles. Analytical electron microscopy (AEM) analyses were performed on particles of smectite after Ca^{2+} saturation or in the natural state of saturation. Both the individual and the average structural formulae presented in Table 2 were calculated for O10 (OH)2, assuming that all Fe is in the ferric state (as expected from the XRD $d_{06,33}$ values and the IR data) and Mg in the octahedral sheets of the smectite layers (as expected from Ca^{2+} saturation).

All the Ca^{2+}-saturated smectite particles have a similar structural formula, characteristic of a dioctahedral smectite with octahedral occupancy ranging from 2.0 to 2.1 atoms per formula unit (a.p.f.u.) in which the tetrahedral sheet is almost exclusively occupied by Si^{4+} (3.94 to 3.96 a.p.f.u., average). They are very poor in Al, <0.10 a.p.f.u essentially substituted for Si in tetrahedral sheets, and Fe^{3+} (from 1.27 to 1.52 a.p.f.u.) largely predominates over Mg (~0.6 a.p.f.u.) in the octahedral sheet. The total negative charge of the 2:1 layer (0.43−0.53, average) is essentially due to Mg^{2+} for Fe^{3+} substitutions in the octahedral sheets. Plotted in the $4Si-\Sigma^{VI}Fe$ diagram (Figure 7) modified from Meunier *et al.* (2003), the chemical compositions of the smectite are grouped in the Fe-montmorillonite domain (Fe-rich smectite with a dominant octahedral charge).

Comparison of the AEM analyses of smectite particles from 27-52R in its natural state with those obtained after Ca^{2+} saturation (Table 2) indicates that some of the K^+ and Na^+ cations which compensated the layer charge of the natural smectite still persist after Ca^{2+} saturation. The presence of non-exchangeable K^+, Na^+ interlayer cations is consistent with the non-swelling collapsed layers previously detected by XRD.

A detailed examination of the layer charge calculated from the structural formulae (Figure 8) indicates a wide range of variations ranging from low-charge to high-charge smectites (0.2−0.7 per half unit-cell) in which most of the negative charge is always octahedral. Such a range of variation has already been reported for dioctahedral Fe^{3+}-rich smectite samples from the weathering of ultrabasic rocks in Australia (Gaudin *et al.*, 2004a). No compositional trend towards the high-charged glauconite mica domain is observed in Figure 8. This suggests that the non-swelling layers of the mixed-layer particles probably correspond to collapsed K^+, Na^+-rich smectite layers and not to glauconite layers. Moreover, the absence of a correlation between

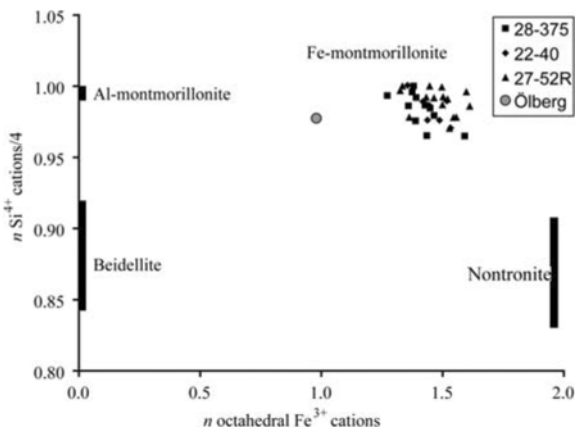

Figure 7. TEM-EDX analyses of Ca^{2+}-saturated smectite particles reported in the $4Si-\Sigma^{VI}Fe$ diagram (modified from Meunier, 2003). Gray circle: Fe-montmorillonite from Ölberg (Köster *et al.*, 1999).

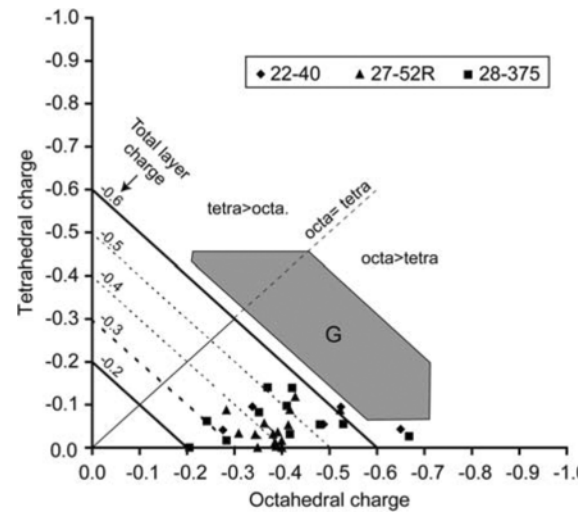

Figure 8. Tetrahedral charge *vs.* octahedral charge of the smectite particles (TEM-EDX analyses). G: mica glauconite domain from the ternary charge distribution diagram established by Köster (1982) (Figure 10). Tetra: tetrahedral charge, octa: octahedral charge.

https://doi.org/10.1346/CCMN.2005.0530503 Published online by Cambridge University Press

Table 2. Structural formulae of the smectites calculated from TEM-EDX data (average for each sample analyzed and individual smectite particles).

Sample	IV Si^{4+}	IV Al^{3+}	IV Fe^{3+}	VI Fe^{3+}	VI Al^{3+}	VI Mg^{2+}	VI Mn^{2+}	Interf. cations K^+	Interf. cations Ca^{2+}	Interf. cations Na^+	Layer charge	Octa. ch. %	$\Sigma^{VI}R$
Average Ca^{2+}-saturated <2 μm fractions													
22-40	3.94	0.06	–	1.46	–	0.56	0.02	0.07	0.15	0.17	–0.53	88	2.04
27-52R	3.96	0.02	0.02	1.46	–	0.61	0.01	0.08	0.15	0.06	–0.43	90	2.08
28-375	3.94	0.06	–	1.41	0.02	0.65	0.01	0.17	0.09	0.10	–0.46	87	2.08
Average smectite from bulk samples (not saturated with Ca^{2+})													
27-52R	3.94	0.04	0.02	1.42	–	0.68	0.02	0.11	0.11	0.07	–0.40	88	2.12
TEM-EDX analyses of individual Ca^{2+}-saturated smectite particles													
22-40	3.90	0.08	0.02	1.47	–	0.61	0.01	0.06	0.08	0.21	–0.43	78	2.10
	4.00	–	–	1.36	0.08	0.58	0.02	0.05	0.11	0.22	–0.48	101	2.04
	3.90	0.08	0.01	1.43	–	0.58	0.02	0.11	0.15	0.21	–0.62	85	2.03
	3.95	0.05	–	1.45	–	0.57	0.02	0.07	0.16	0.16	–0.54	90	2.03
	3.88	0.04	0.07	1.46	–	0.53	0.01	0.05	0.23	0.16	–0.66	82	2.00
	3.96	0.04	–	1.52	0.01	0.56	0.01	0.05	0.12	0.03	–0.32	87	2.10
	3.96	0.04	–	1.42	–	0.53	0.01	0.08	0.22	0.18	–0.69	94	1.96
27-52R	3.91	0.02	0.07	1.30	–	0.77	0.02	0.10	0.11	0.28	–0.61	86	2.09
	3.91	0.03	0.05	1.50	–	0.60	–	0.06	0.11	0.10	–0.37	76	2.11
	3.97	0.02	0.01	1.49	–	0.57	0.02	0.04	0.10	0.13	–0.37	92	2.08
	3.99	0.01	–	1.33	0.03	0.76	0.02	0.04	0.09	0.17	–0.40	97	2.13
	4.00	0.00	–	1.50	–	0.55	0.01	0.09	0.12	0.06	–0.39	99	2.06
	3.88	0.06	0.06	1.47	–	0.58	0.01	0.12	0.17	0.09	–0.55	78	2.05
	3.97	0.02	0.01	1.45	–	0.67	–	0.04	0.15	0.01	–0.34	90	2.12
	3.94	0.01	0.05	1.57	–	0.47	–	0.06	0.18	0.00	–0.42	87	2.04
	4.00	–	–	1.33	0.04	0.72	0.01	0.09	0.15	0.01	–0.40	100	2.10
	4.00	–	–	1.45	0.01	0.62	–	0.06	0.15	0.00	–0.35	100	2.07
	3.97	0.03	–	1.43	–	0.66	–	0.04	0.18	0.01	–0.41	92	2.09
	3.91	–	0.09	1.46	–	0.61	–	0.28	0.10	0.01	–0.50	83	2.06
	3.95	0.02	0.04	1.46	–	0.60	–	0.03	0.21	0.02	–0.47	89	2.06
	3.98	–	0.02	1.58	–	0.43	–	0.02	0.20	0.00	–0.42	96	2.01
	3.96	–	0.04	1.48	–	0.58	–	0.04	0.19	0.01	–0.43	91	2.06
28-375	3.98	0.02	–	1.38	0.03	0.75	0.01	0.10	0.09	0.02	–0.30	95	2.16
	3.90	0.09	0.01	1.38	–	0.73	0.00	0.26	0.08	0.09	–0.51	81	2.11
	4.00	–	–	1.38	0.08	0.67	0.02	0.09	0.01	0.09	–0.21	100	2.15
	3.92	0.08	–	1.47	0.02	0.59	0.00	0.18	0.09	0.07	–0.43	81	2.08
	3.86	0.10	0.04	1.40	–	0.69	0.01	0.28	0.10	0.08	–0.56	75	2.09
	3.97	0.03	–	1.39	0.04	0.63	0.01	0.16	0.10	0.08	–0.45	93	2.08
	3.94	0.06	–	1.45	0.02	0.67	0.01	0.17	0.02	0.10	–0.30	80	2.14
	3.95	0.05	–	1.43	–	0.61	0.01	0.18	0.15	0.05	–0.53	90	2.04
	3.97	0.03	–	1.27	0.07	0.66	0.00	0.06	0.20	0.23	–0.69	96	2.00
	3.94	0.06	–	1.36	0.06	0.59	0.01	0.20	0.09	0.21	–0.58	91	2.03
	3.86	0.07	0.07	1.52	–	0.53	0.00	0.20	0.10	0.12	–0.51	73	2.05

the K^+ content and the total layer charges supports the collapsed smectite layer hypothesis (Table 2).

FTIR spectroscopy. The IR spectra of the smectite samples collected from deep-sea drilling in the Costa Rica margin (Figure 9a) are very similar to that of the Ölberg Fe-montmorillonite originating from the weathering of peridotite nodules (Köster *et al*., 1999; Petit *et al*., 2002). In the OH-bending region, the major band at 820 cm^{-1} is classically attributed to $\delta Fe^{3+}Fe^{3+}\square$–OH vibration (*e.g*. Farmer, 1974). The well resolved band at 761 cm^{-1} is attributed to $\delta Fe^{3+}Mg$'–OH vibration in Fe-montmorillonites (Petit *et al*., 2002; Gaudin *et al*., 2004b). Only one absorption band at 687 cm^{-1}, assigned to Fe^{3+}–O out-of-plane vibration (Bishop *et al*., 2004a, 2004b), is noted in the 600–750 cm^{-1} region. The broad asymmetric band at 3554 cm^{-1} observed in the OH-streching region is due to the superimposition of several individual bands, in particular $\nu Fe^{3+}Fe^{3+}$–OH and $\nu Fe^{3+}Mg$–OH, located at ~3550 cm^{-1} and 3575 cm^{-1} (Farmer, 1974; Goodman *et al*., 1976; Petit *et al*., 2002). A weak shoulder is noted near 3640 cm^{-1}. Such a band was attributed to vibrations of water in the Ölberg Fe-montmorillonite (Petit *et al*., 2002), but the existence of νMg_2Fe^{3+}–OH and $\nu MgFe_2^{3+}$–OH vibrations in the 3660–3630 cm^{-1} region was also suggested by the authors. The presence of such bands is consistent with octahedral occupancies slightly >2 estimated from

https://doi.org/10.1346/CCMN.2005.0530503 Published online by Cambridge University Press

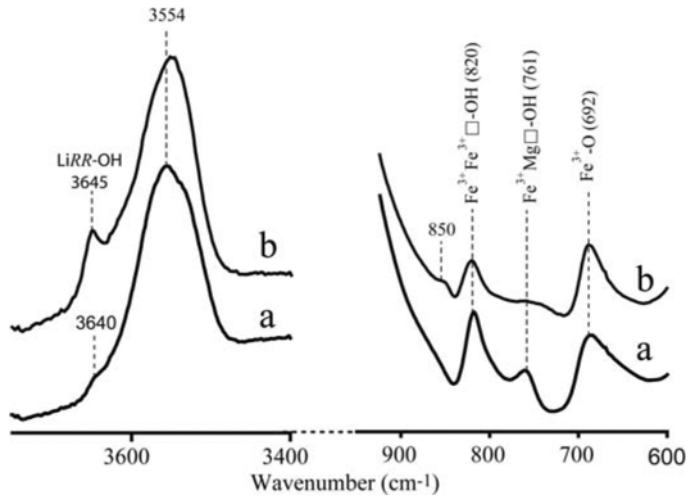

Figure 9. FTIR spectra of sample 27-52R (OH-bending and OH-stretching region): (a) before HK treatment, (b) after HK treatment.

the structural formulae and could be due to the presence of small amounts of trioctahedral clusters in the dioctahedral sheets of the Fe-montmorillonite.

The occurrence of $\delta Fe^{3+}Mg\square-OH$ bands indicates that Fe and Mg cations occur in adjacent octahedra within the same sheet of the smectite layers. In agreement with AEM analyses, this confirms that the Fe^{3+}, Mg^{2+}-rich compositions of the smectites do not result from a mixing of Fe^{3+}-rich and Mg^{2+}-rich individual particles or layers.

HK-treated samples. During neutralization of octahedral charges by HK treatment, Li^+ cations migrate from the interlayer exchangeable positions into the formerly vacant octahedra. According to the structure of dioctahedral smectites, migration of one Li^+ cation into a vacant octahedral site should affect two OH groups directed initially towards the vacant site (Calvet and Prost, 1971). Consequently, some OH groups with dioctahedral environment are affected and OH groups with trioctahedral coordination such as $R^{3+}R^{3+}Li^+-OH$, $R^{3+}R^{2+}Li^+-OH$ or $R^{2+}R^{2+}Li^+-OH$ may be created. In this study, the structural changes of the HK-treated samples are characterized by the appearance of only one intense band at 3645 cm^{-1} in the OH-stretching region (Figure 9b). For the HK-treated Ölberg Fe-montmorillonite (Petit *et al*., 2002), the appearance of three bands at 3609 cm^{-1}, 3645 cm^{-1} and 3672 cm^{-1} were observed by Petit *et al*. (2002) and were attributed to νLiR_2-OH vibrations (R being Al^{3+}, Fe^{3+}, Mg^{2+}). However, as the octahedral chemistry of the smectite studied is simpler here, the appearance of only one band at 3645 cm^{-1} after HK treatment is attributed to $\nu Fe^{3+}Fe^{3+}Li-OH$ vibration. In the OH-bending region, a decrease in the relative intensities of $\delta Fe^{3+}Fe^{3+}-OH$, $\delta Fe^{3+}Mg-OH$ bands and the appearance of a new band at 850 cm^{-1} are observed after HK treatment. This last new band was also noted for the HK-treated Ölberg Fe-montmorillonite (Petit *et al*., 2002) but no accurate assignment was proposed by the authors.

The proportion of the octahedral charge of the smectites was measured by FTIR spectroscopy using the method established by Petit *et al*. (1998). This method is based on the quantitative measurement of the amounts of NH_4^+ in NH_4-saturated smectites before and after the neutralization of the octahedral charge by Li fixation. For most of the samples, the results indicate octahedral charge proportions varying between 41 and 60% of the total layer charge. These values are significantly lower than those calculated from structural formulae which are $\geqslant$87% (Table 2). According to the previous AEM results which have shown that non-exchanged interlayer K^+ and Na^+ cations persist in the Fe-montmorillonite after Ca^{2+} saturation, it seems reasonable to expect the same behavior after Li^+ saturation. Thus, the octahedral charges of such smectite layers were probably not fully compensated by Li^+ fixation after HK treatment. This could explain the apparent underestimation of the octahedral charge proportion of smectites using the spectroscopic method. Moreover, this could also explain the large amounts of swelling smectite layers detected by XRD after HK treatment, although the amount of the smectite tetrahedral charges calculated from AEM analyses is very small.

DISCUSSION

Nature of smectite in green grains

The zoning of the green grains formed in the upper bioturbated zones of the deep-sea calcareous sediments near the Costa Rica margin is the product of two distinctive processes: (1) early pyritization of the organic matter by microbial reduction; and (2) later dissolution then replacement of pyrite by smectite associated with minor Fe oxides.

https://doi.org/10.1346/CCMN.2005.0530503 Published online by Cambridge University Press

The XRD, TEM-EDX and FTIR data indicate that the smectite present has the crystal-structure and the crystal-chemical characteristics of a montmorillonite with the following average structural formula (27-52R sample, Table 2): $^{IV}(Si_{3.94}Al_{0.04}Fe^{3+}_{0.02})^{VI}(Fe^{3+}_{1.42}Mg_{0.68}Mn_{0.02})O_{10}(OH)_2(K_{0.11}Ca_{0.11}Na_{0.07}.nH_2O)$.

The detection of non-swelling layers by XRD is related to the collapse of Na^+ or K^+ interlayer in smectite particles. This behavior induces incomplete exchange after Ca^{2+} and Li^+ saturation experiments.

Plotted in the ternary charge-distribution diagram established by Köster (1982), most of the analyzed smectite samples fall in or close to the Fe-montmorillonite domain (Figure 10). Fe-montmorillonite is rarely reported in the literature, most of the Fe-rich smectites usually being described as nontronites (Fe-rich smectite with a dominant tetrahedral charge). An Fe-montmorillonite from Ölberg was described by Köster *et al.* (1999) and Petit *et al.* (2002) as a clay product of the weathering of peridotite nodules and was considered by the authors as a rare exception. More recently, Gaudin *et al.* (2004a) reported large lateritic profiles 10–15 m thick and kilometres wide, partly composed of Fe-montmorillonite particles and developed also from weathering of peridotites. Based on the common context of formation of the Murrin Murrin and Ölberg Fe-montmorillonites, Gaudin *et al.* (2004a) suggested that this peculiar type of smectite is a specific clay product of the weathering of the ultrabasic rocks. Nevertheless, in an oceanic environment, although nontronites are frequently observed as the smectite glauconite end-member, Buatier *et al.* (1993) and Wiewióra *et al.* (2001) identified an Fe-montmorillonite formation as the precursor mineral of the glauconite mica in marine sediments. Consequently, this study confirms that the Fe-montmorillonite does not occur exclusively as a weathering product of ultrabasic rocks but also occurs as a newly formed mineral in the alteration of deep-water marine sediments. Moreover, the rare Fe-montmorillonites reported in the literature often display greater Al contents (see "Ölberg" in Figure 7) and/or higher tetrahedral charges than those of the present study (Figure 10). Thus, a major result of this investigation was to reveal the occurrence of nearly pure Fe-montmorillonites formed in deep-water sediments.

Mechanisms of formation of Fe-montmorillonite

Petrographic observations of the grains scattered within the carbonated oozes indicate that their zoning results from the progressive inward alteration and replacement of the euhedral pyrite aggregates by Fe-montmorillonites. Thus, the formation of such grains could be explained by two successive diagenetic redox stages (Figure 11):

1 – Reducing stage (Figure 11a,b). Pyrite precipitates in micro-reducing environments distinct from the surrounding sediments. For this reason, newly-formed pyrite in

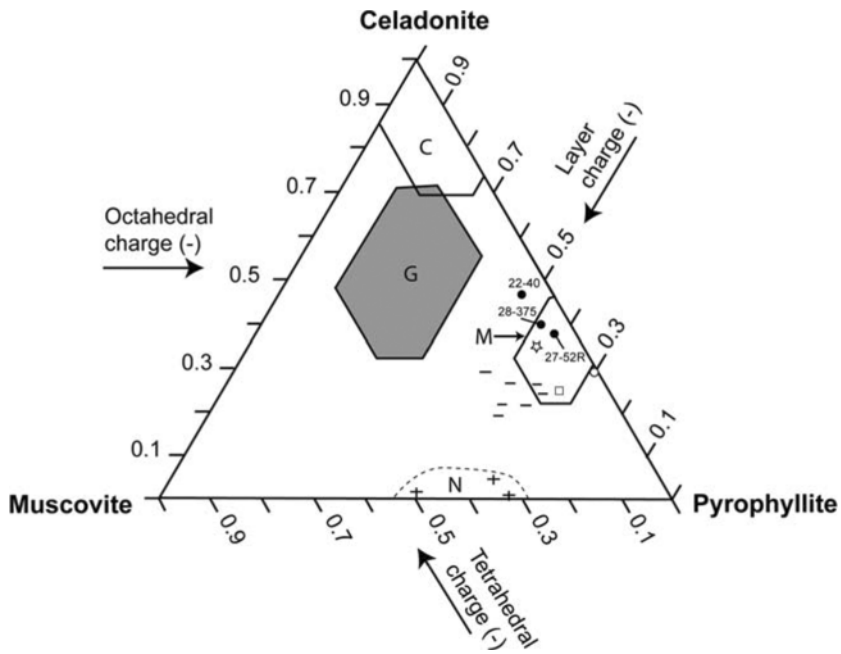

Figure 10. Average charge distribution of the smectite samples (average TEM-EDX analyses) reported in the charge-distribution diagram established by Köster (1982). G: glauconite mica domain, M: montmorillonite domain, N: nontronite domain (+: nontronite from Koster *et al.* (1999)). Fe-montmorillonites from the literature are reported: ☆: Ölberg Fe-montmorillonite (Köster *et al.*, 1999); – : Australian smectites issued from weathering profiles developed from peridotites (Gaudin *et al.*, 2004a); ○: Fe-montmorillonite as initial product of glauconite from the Ivory Coast-Ghana ridge (Wiewióra *et al.*, 2001); □: Fe-montmorillonite from the Galapagos Spreading Centre hydrothermal mounds (average TEM-EDX analyses) (Buatier *et al.*, 1993).

https://doi.org/10.1346/CCMN.2005.0530503 Published online by Cambridge University Press

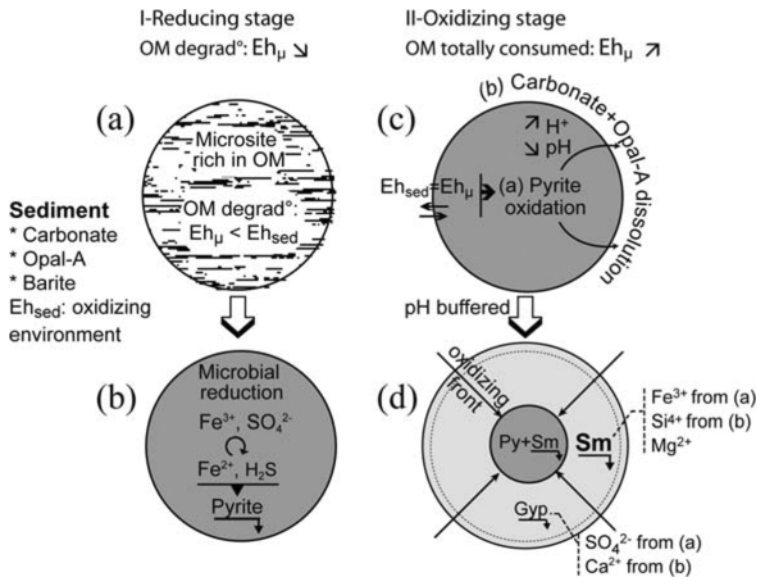

Figure 11. Diagram showing an interpretation of the formation of the pyritic and smectitic grains within the pelagic carbonated sediments.

very shallow-buried marine sediments is widely reported in the literature. This formation is commonly attributed to early diagenetic processes, and more particularly to degradation of the organic matter and to bacterial reducing processes (Larsen and Chilingar, 1967; Fairbridge, 1967; Berner, 1984; Wilkin and Barnes, 1997; Kelly and Webb, 1999; Shen and Buick, 2004, *etc.*). The organic matter provides nutrients for development of anaerobic reducing bacteria. Thus, microsites rich in organic matter may be sites of high sulfide and ferrous Fe production by sulfate and ferric iron-reducing bacteria. This leads to local precipitation of aggregates of pyrite octahedra, determined as an early component of the green grains in this study. Indeed, the huge number of very small pyrite octahedra and the small framboïdal pyrite occurrences observed within the grains are usually considered as typical textures resulting from the pyritization of organic material in early diagenetic environments (Love, 1967; Wilkin and Barnes, 1997; McKay and Longstaffe, 2003). Moreover, we notice here that barite minerals and SO_4^{2-} anions from the seawater may provide the main sulfur source necessary for pyrite formation.

2 – Oxidizing stage (Figure 11b,c). Pyrite grains are progressively dissolved and replaced by Fe^{3+}-montmorillonites from the rim to the core of the grains. This implies a redox change from reducing conditions to more oxidizing conditions. This probably results from the cessation of bacterial reducing processes related to the total consumption of the organic matter initially present in the microenvironments. Then the local redox conditions are rebalanced with the oxidizing surrounding sediments. The effect of this is the appearance of an oxidation front evolving progressively from the rim to the inner part of the grains. In response to this redox change, pyrite which was stable under reducing conditions becomes unstable and is gradually dissolved following the reaction:

$$2FeS_2 + 15/2O_2 + H_2O \rightarrow 2Fe^{3+} + 4SO_4^{2-} + 2H^+$$

The local production of H^+ resulting from this reaction is buffered by the dissolution of carbonate bioclasts surrounding the pyritic microenvironments. These buffered pH conditions allow the precipitation of smectites. Thus, Fe^{3+} cations released from the pyrite oxidation react with Si from dissolved biogenic opal and Mg from seawater or sediments to produce new stable authigenic Fe^{3+}, Mg-rich montmorillonites in replacement of dissolved pyrites and carbonate bioclasts (Figure 4). The TEM observations of the smectite-pyrite interfaces suggest that the replacement of pyrites by smectite occurs through a dissolution-precipitation process with the formation of an X-ray amorphous intermediate product (a gel). Moreover, $SO_4^{2-}$and Ca^{2+} cations released from the pyrite and carbonate dissolution react to form gypsum detected within some grains (Table 1).

Occurrence of green grains in other marine environments

This study highlights the formation of authigenic Fe^{3+}-montmorillonites related to early diagenetic processes in deep-water (3000 m) sediments. In marine sediments, smectite layers usually occur within mixed-layer clays, as smectite-glauconite or smectite-illite clays. Therefore, it is most likely that Fe-montmorillonite, not interstratified with illite or glauconite layers, is thermodynamically unstable during the marine diagenesis.

https://doi.org/10.1346/CCMN.2005.0530503 Published online by Cambridge University Press

The reason why the nature of the clays of the green grains is exclusively montmorillonitic is yet to be determined.

A first hypothesis to explain the absence of glauconite would be that the formation of Fe-montmorillonite depends on a specific mechanism of formation (*i.e.* replacement of diagenetic pyrite in deep-water pelagic, carbonated and siliceous sediments in the absence of parental Al-silicate). Such a mechanism has never been proposed for the formation of glauconite and when observed in glauconite-bearing sediments, pyrite generally postdates the formation of glauconite (Giresse and Wiewióra, 2001; Kelley and Webb, 1999).

A second hypothesis would be that crystallization of Fe-montmorillonite corresponds to the first step of an overall glauconitization process including Fe-montmorillonite-to-glauconite conversion *via* glauconite-smectite mixed-layer minerals. In that case, Fe-montmorillonite would be a temporary mineral phase the persistence of which is controlled not only by chemical (availability of Al and K) and thermal (very low temperature) conditions but also by reaction kinetics.

Several authors have already discussed the influence of time on the glauconitization process. Odin and Matter (1981) specified that the degree of evolution of the glauconite (nascent, little-evolved, evolved and highly-evolved glauconite) increases with the time of residence of the green grains at the sea bottom before burial. The glauconitization process generally occurs at 60–500 m water depth. At greater depths, the energy is lower (low temperature) and the burial process is more continuous and effective and the glauconitization is generally inhibited (Odin and Morton, 1988; Wiewióra *et al.*, 2001). However, a few glauconitization processes have been reported in deep-water sediments (Odin and Morton, 1988). Wiewióra *et al.* (2001) described a glauconitization process in pelagic formaminifer chambers from superficial sediments at 2100 m water depth and a 3ºC water temperature. These authors described the formation of a first Fe-montmorillonite which could evolve towards the glauconite end-member. They also explained the occurrence of glauconite in this deep-sea environment (2100 m water depth, 3ºC water depth) by the presence of a "deep current activity". This would "cause winnowing of fine particles, and such reworking allows exposure of green grains at the sea floor for periods sufficient to cause ionic exchange at the sediment-water interface".

Therefore, we suggest that the occurrence of the Fe-montmorillonite which forms the green grains from the Costa Rica margin could belong to an incipient glauconitization process in deep-sea conditions. The persistence of Fe-montmorillonite in such a geological environment could be explained by the young age of the sediments, the absence of strong bottom currents during their formation and of course by the low temperature (~2ºC) of the sea water at 3000 m depth. In those conditions, the rate of chemical reaction is much slower in the shallowest environments (60–500 m, ~15ºC) and the transformation of the Fe-montmorillonite to mixed-layer glauconite-smectite is still not effective.

This study has allowed us to define pyrite as a source mineral for the occurrence of authigenic Fe-montmorillonites in deep-water carbonated and siliceous sediments. This process of Fe-rich clay formation probably exists over a wide extent in the deep-sea floor, *e.g.* Tamburini *et al.* (2003) reported the occurrence of green clay layers in the bioturbated zones of the upper part of marine sediments at 2000–3300 m water depth in the South China Sea during ODP leg 184. Their XRD study indicated smectites with no evidence of glauconite and "in many occurrences a clear association with iron sulfide minerals and pyrite nodules was found" (Tamburini *et al.*, 2003). It is most likely that the nature of the smectites from these green clay layers and their mechanism of formation are quite similar to those described in the present study.

CONCLUSIONS

This study reveals the occurrence of authigenic Fe^{3+}-montmorillonite accurately identified by XRD, FTIR and TEM-EDX in calcareous pelagic sediments located at 3000 m below sea level. The formation of such Fe^{3+}-montmorillonite is suggested to be related to successive diagenetic redox stages. The Fe^{3+} and Si^{4+} are provided by the dissolution of pyrite and biogenic opal. The Fe^{3+}-montmorillonite formation in deep-marine sediments, rarely described in the literature, could belong to an incipient glauconitization process in deep-water conditions.

ACKNOWLEDGMENTS

M.D.B. thanks Geoff Wheat and Andy Fisher for their invitation to join the *Ticoflux II* expedition. The authors thank D. Proper and M. Ergel (UFC Besançon) who impregnated and cut the samples for TEM work. The authors used the Jeol-2000fx electron microscope of the CRMC2 facilities for electron microscopy: assistance on the machine by Serge Nitshe is very much appreciated. The authors are grateful to Claude Fontaine for his help with preparation of samples for analyses and François Martin for taking part in this study. Thanks also to Andrzej Wiewióra and David Hradil for their helpful reviews of the paper. This work was supported by INSU ocean program (MDB), by the national facility INSU program (TEM from Marseille) and by NSF grant 0002031 (*Ticoflux* expedition).

REFERENCES

Berner, R.A. (1984) Sedimentary pyrite formation: an update. *Geochimica et Cosmochimica Acta*, **48**, 605–615.

Bishop, J., Madejová, J., Komadel, P. and Fröschl, H. (2002a) The influence of structural Fe, Al and Mg on the infrared OH bands in spectra of dioctahedral smectites. *Clay Minerals*, **37**, 607–616.

Bishop, J., Murad, E. and Dyar, M.D. (2002b) The influence of octahedral and tetrahedral cation substitution on the

structure of smectites and serpentines as observed through infrared spectroscopy. *Clay Minerals*, **37**, 617–628.

Buatier, M.D., Ouyang, K. and Sanchez, J.P. (1993) Iron in hydrothermal clays from the Galapagos spreading centre mounds: consequences for the clay transition mechanism. *Clay Minerals*, **28**, 641–655.

Calvet, R. and Prost, R. (1971) Cation migration into empty octahedral sites and surface properties of clays. *Clays and Clay Minerals*, **19**, 175–186.

Elsass, F., Beaumont, A., Pernes, M., Jaunet, A.M. and Tessier, D. (1988) Changes in layer organization of Na and Ca exchanged smectite during solvent exchange for embedment in resin. *The Canadian Mineralogist*, **36**, 1325–1333.

Fairbridge, R.W. (1967) Phases of diagenesis and authigenesis. Pp. 19–89 in: *Developments in Sedimentology* (G. Larsen and G.V. Chilingar, editors). *Diagenesis in Sediments*, **8**. Elsevier, Amsterdam.

Farmer, V.C. (1974) The layer silicates. Pp. 331–365 in: *The Infrared Spectra of Minerals* (V.C. Farmer, editor). Monograph **4**, Mineralogical Society, London.

Fisher, A.T., Stein, C.A., Harris, R.N., Wang, K., Silver, E.A., Pfender, M., Hutnak, M., Cherkaoui, A., Bodzin, R. and Villinger, H. (2003) Abrupt thermal transition reveals hydrothermal boundary and role of seamounts within the Cocos Plate. *Geophysical Research Letters*, **30**, 1–4.

Gaudin, A., Grauby, O., Noack, Y., Decarreau, A. and Petit, S. (2004a) Accurate crystal chemistry of ferric smectites from the lateritic nickel ore of Murin Murin (Western Australia). I. XRD and multi-scale chemical approaches. *Clay Minerals*, **39**, 301–315.

Gaudin, A., Petit, S., Rose, J., Martin, F., Decarreau, A., Noack, Y. and Borschneck, D. (2004b) Accurate crystal chemistry of ferric smectites from the lateritic nickel ore of Murin Murin (Western Australia). II Spectroscopic (IR and EXAFS) approaches. *Clay Minerals*, **39**, 453–467.

Giresse, P. and Wiewióra, A. (2001) Stratigraphic condensed deposition and diagenetic evolution of green clay minerals in deep water sediments on the Ivory Coast-Ghana Ridge. *Marine Geology*, **179**, 51–70.

Goodman, B.A., Russell, J.D., Fraser, A.D. and Woodhams, F.W.D. (1976) A Mössbauer and IR spectroscopic study of the structure of nontronite. *Clays and Clay Minerals*, **24**, 53–59.

Hofmann, U. and Klemen, R. (1950) Vrelust der Austauschfahgkeit von Lithiumionen an Bentonit durch Erhitzung. *Zeitschrift für Anorganische und Allgemeine Chemie*, **262**, 95–99.

Kelly, J.C. and Webb, J.A. (1999) The genesis of glaucony in the Oligo-Miocene Torquay Group, southeastern Australia: petrographic and geochemical evidence. *Sedimentary Geology*, **125**, 99–114.

Köster, H.M. (1982) The crystal structure of 2:1 layer silicates. *Proceedings of the International Clay Conference, Bologna-Pavia*, 41–71.

Köster, H.M., Ehrlicher, U., Gilg, H.A., Jordan, R., Murad, E. and Onnich, K. (1999) Mineralogical and chemical characteristics of five nontronite and Fe-rich smectites. *Clay Minerals*, **34**, 579–599.

Lanson, B. (1993) *DECOMPXR, X-ray Decomposition Program*. ERM, Poitiers, France.

Larsen, G. and Chilingar, G.V. (1967) Introduction. Pp. 1–17 in: *Diagenesis in Sediments* (G. Larsen and G.V. Chilingar, editors). Developments in Sedimentology, **8**. Elsevier, Amsterdam, The Netherlands.

Love, L.G. (1967) Early diagenetic iron sulphide in Recent sediments of the Wash, England. *Sedimentology*, **9**, 327–352.

McKay, J.L. and Longstaff, F.J. (2003) Sulphur isotope geochemistry of pyrite from the Upper Cretaceous Marshybank formation, Western Interior Basin. *Sedimentary Geology*, **157**, 175–195.

Meunier, A. (2003) *Argiles*. Société géologique de France, GB Science Publisher, France.

Odin, G.S. and Fullagar, P.D. (1988) Geological significance of the glaucony facies. Pp. 295–332 in: *Green Marine Clays* (G.S. Odin, editor). Developments in Sedimentology, **45**. Elsevier, Amsterdam.

Odin, G.S. and Matter, A. (1981) De glauconiarium originae. *Sedimentology*, **28**, 614–641.

Odin, G.S. and Morton, A.C. (1988) Authigenic green particles from marine environments. Pp. 213–264 in: *Developments in Sedimentology* (G.V. Chilingarian and K.H. Wolf, editors). Diagenesis II, **43**. Elsevier , Amsterdam.

Petit, S., Righi, D., Madejová, J. and Decarreau, A. (1998) Layer charge estimation of smectites using infrared spectroscopy. *Clay Minerals*, **33**, 579–591.

Petit, S., Caillaud, J., Righi, D., Madejová, J., Elsass, F. and Köster, H.M. (2002) Characterization and crystal chemistry of an Fe-rich montmorillonite from Ölberg, Germany. *Clay Minerals*, **37**, 283–297.

Reynolds, R.C. (1985) *NEWMOD*: *A computer program for the calculation of the basal diffraction intensities of mixed-layered clay minerals*. R.C. Reynolds, 8 Brook Rd, Hanover, New Hampshire, USA.

Shen, Y. and Buick, R. (2004) The antiquity of microbial sulfate reduction. *Earth-Science Reviews*, **64**, 243–272.

Suquet, H., Malard, C., Copin, E. and Pezerat, H. (1981a) Variation du paramètre b et de la distance basale d_{001} dans une série de saponites à charge croissante: I. Etats hydratés. *Clay Minerals*, **16**, 53–67.

Suquet, H., Malard, C., Copin, E. and Pezerat, H. (1981b) Variation du paramètre b et de la distance basale d_{001} dans une série de saponites à charge croissante: II. Etats 'zéro couche'. *Clay Minerals*, **16**, 181–193.

Tamburini, F., Adatte, T. and Föllmi, K.B. (2003) Origin and nature of green clay layers, ODP leg 184, South China Sea. *Proceedings of the Ocean Drilling Program, Scientific Results*, **184**, 1–23.

Tessier, D. (1984) Hydratation, gonflement et structuration des matériaux argileux au cours de la dessication et de la réhumectation. PhD thesis, Université de Paris & INRA Versailles, France, 361 pp.

Wiewióra, A., Giresse, P., Petit, S. and Wilamowski, A. (2001) A deep-water glauconitization process on the Ivory Coast-Ghana marginal ridge (ODP site 959): determination of Fe^{3+}-rich montmorillonite in green grains. *Clays and Clay Minerals*, **49**, 540–558.

Wilkin, R.T. and Barnes, H.L. (1997) Formation processes of framboidal pyrite. *Geochimica et Cosmochimica Acta*, **61**, 323–339.

(*Received 9 March 2005; revised 27 May 2005; Ms. 1023*)